

Integration of coherence and volumetric curvature images

SATINDER CHOPRA, Arcis Corporation, Calgary
KURT J. MARFURT, University of Oklahoma

Volumetric attributes computed from 3D seismic data are powerful tools in the prediction of fractures and other stratigraphic features. Geologic structures often exhibit curvature of different wavelengths, providing different perspectives of the same geology. Tight (short-wavelength) curvature delineates details within intense, highly localized fracture systems. Broad (long-wavelength) curvature usually enhances subtle flexures on the scale of 100–200 traces that are difficult to see in conventional seismic, but often correlate to fracture zones below seismic resolution, and also collapse features and diagenetic alterations that result in broader bowls. We present a number of curvature examples demonstrating their interpretational value.

Introduction

Computation of volumetric curvature attributes from seismic data is a significant advance in the field of attributes. Initial curvature applications were limited to picked 3D seismic horizons. In addition to delineating faults (Sigismundi and Soldo, 2003) and subtle carbonate buildups (Hart and Sagan, 2005), horizon-based curvature has been correlated to open fractures measured on outcrops (Lisle, 1994) and to production data (Hart et al., 2002). Horizon-based curvature is limited not only by the interpreter's ability to pick events, but also by the existence of horizons of interest at the appropriate level in 3D seismic data volumes. Horizon picking can be a challenging task in data sets contaminated with noise and where rock interfaces do not exhibit a consistent impedance contrast amenable to human interpretation. To address this issue, Al-Dossary and Marfurt (2006) generated volumetric estimates of curvature from volumetric estimates of reflector dip and azimuth. Such reflector dip and azimuth estimates can be calculated using a complex trace analysis (Barnes, 2000), a gradient-structure tensor (Randen et al., 2000), discrete semblance-based searches (Marfurt 2006), or plane-wave destructor techniques (Fomel, 2008). Computing derivatives of the volumetric reflector dip components provides a full 3D volume of curvature values. Many curvature measures can be computed, with several workers finding a good correlation between dip, strike curvature (Hart et al.), and Gaussian curvature (Lisle, 1994) to open fractures. In general, curvature is an excellent measure of paleo-deformation. With an appropriate tectonic model, a good structural geologist can predict where fractures were formed. Since their formation, such fractures may have been cemented (Rich, 2008), filled with overlying sediments, or diagenetically altered (Nissen et al., 2009). Furthermore, the present-day direction of minimum horizontal stress may have rotated from the direction at the time of deformation, such that previously open fractures are now closed, while previously closed fractures may now be open. For this reason, predic-

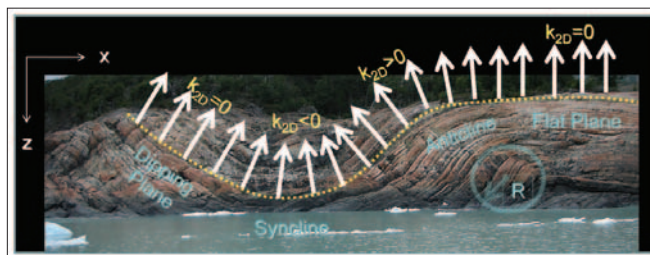


Figure 1. 2D curvature, k_{2D} , is defined as the lateral change of the radius of curvature, R , along a curve, in this case, of folded volcanic strata seen in Perito Moreno Lake, Argentina. White arrows indicate normals to the yellow picked horizon. Anticlinal features have positive curvature and synclinal features negative curvature. Planar (dipping or horizontal) features have zero curvature. (Modified after Roberts, 2001).

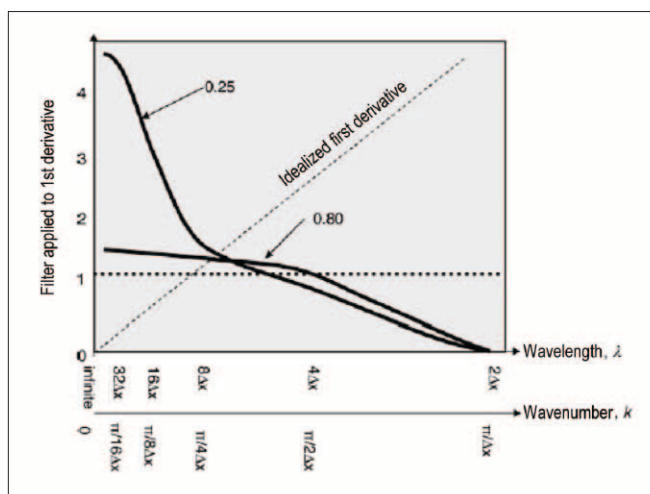


Figure 2. Fractional derivatives visualized as filters applied to the conventional first derivative operator. The idealized derivative is proportional to the wavenumber, k , and inversely proportional to the wavelength, λ . The horizontal dotted line represents a filter applied to the derivative operator that would perfectly reproduce d/dx . Any numerical operator needs to go to zero at Nyquist, or $\lambda = 2\Delta x$. We compensate for coarser sampling artifacts at 45° to the grid by tapering the derivative after $\lambda = 4\Delta x$. The 0.80 derivative slightly enhances the long-wavelength components, while the 0.25 derivative greatly enhances the long-wavelength components. The filters are normalized such that the area under the filtered spectrum (the product of the filter times the idealized first derivative) is equal to 1.0.

tion of open fractures requires not only images of faults and flexures provided by coherence and curvature coupled with an appropriate model of deformation, but also measures of present stress provided by drilling-induced fractures seen in image logs and velocity versus azimuth and amplitude versus azimuth measures computed from surface seismic data.

Many workers will prefer using maximum and minimum curvature (e.g., Sigismundi and Soldo), while others (includ-

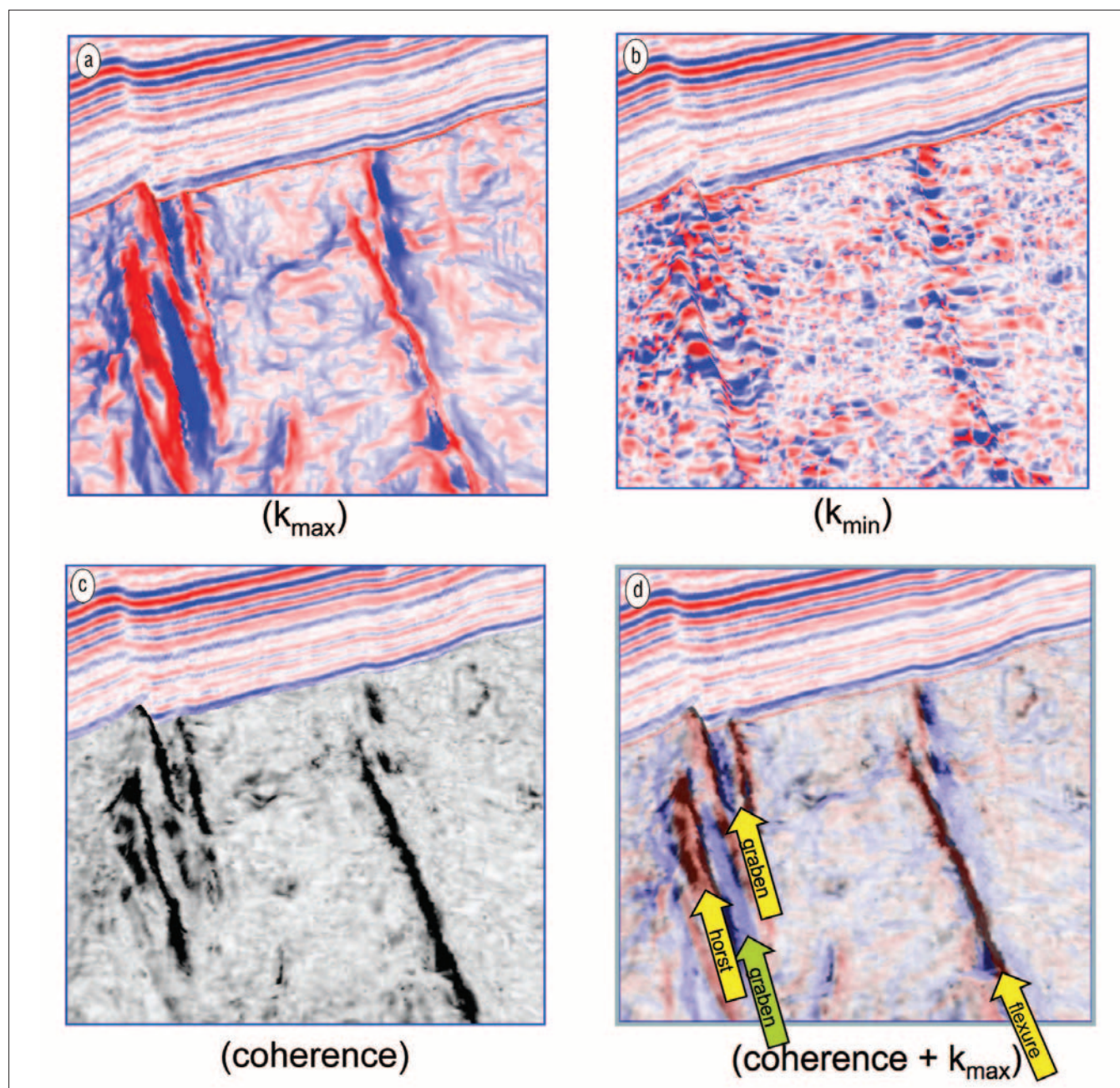


Figure 3. Vertical section through a seismic amplitude volume acquired in Alberta displayed with horizon slices through volumes of (a) maximum curvature, k_{\max} , and (b) minimum curvature, k_{\min} , (c) coherence, and (d) maximum curvature corendered with coherence (opacity = 50%). Many workers like using maximum curvature because they can easily visualize the correlation of upthrown and downthrown faulting with respect to the fault discontinuity.

ing the authors) preferred the most-positive and most-negative curvatures. In this paper, we propose simply using the principal curvatures, k_1 and k_2 , which we describe below. In addition to faults and fractures, stratigraphic features such as levees and bars and diagenetic features such as karst collapse and hydrothermally altered dolomites also appear to be well-defined on curvature displays. Channels appear when differential compaction has taken place.

A review of curvature definitions

Sigismondi and Soldo provide an easy-to-understand defini-

tion of curvature of a 2D surface:

$$k_{2D} = \frac{1}{R} = \frac{\frac{d^2 z}{dx^2}}{\left[1 + \left(\frac{dz}{dx}\right)^2\right]^{3/2}} \quad (1)$$

where R is the radius of curvature and $z(x)$ is the elevation of a 2D horizon (Figure 1). 2D curvature is defined as the change in the radius of curvature, and hence of the angle of the normal with the vertical, $\phi = \tan^{-1}(z/x)$. We raise two

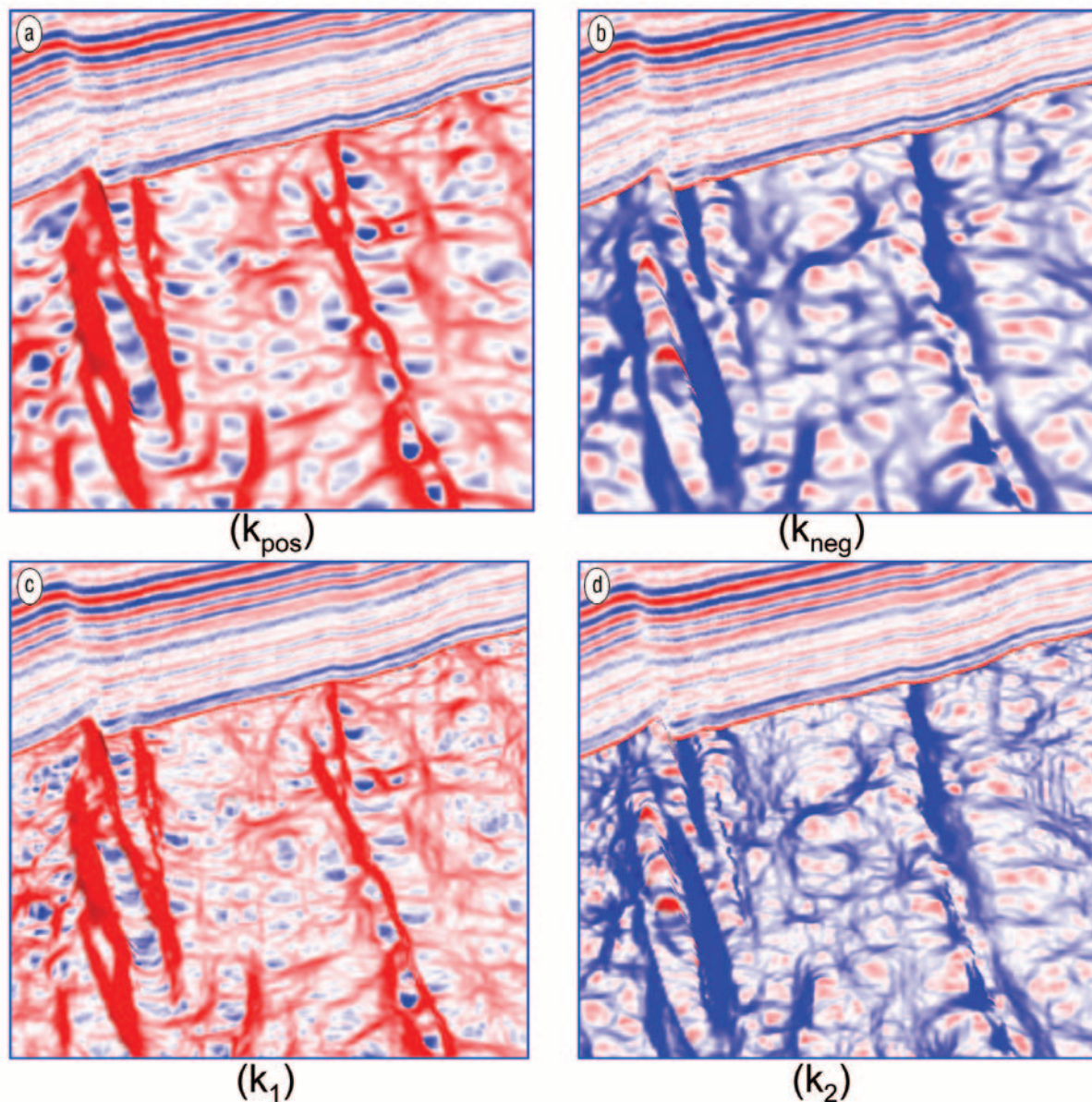


Figure 4. The same vertical section shown in Figure 3, with horizon slices through (a) the most-positive curvature, k_{pos} , (b) the most-negative curvature, k_{neg} , and the two principal curvatures (c) k_1 and (d) k_2 , defined by Equations 6 and 7. k_{pos} and k_{neg} are popular with many interpreters in that they do not suffer the abrupt discontinuities seen in k_{max} and k_{min} which can make subtle lineaments less continuous and mask subtle stratigraphic features. In this paper, we propose using the less commonly used principal curvatures k_1 and k_2 . Like k_{pos} and k_{neg} , k_1 and k_2 show continuous images, but with the advantage that the maximum and minimum values are aligned with the tightest component rather than with the crest and trough of a fold or flexure. Note that k_1 and k_2 contain exactly the same information content as k_{max} and k_{min} shown in Figures 3a and b, but the information is redistributed according to Equations 8 and 9.

pitfalls for those wishing to correlate Equation 1 to curvature definitions found in 3D solid geometry references. First, geoscientists, petroleum engineers, and mining engineers are unique in that they point the positive z or t axis down, rather than up, like the rest of the world. Thus anticlinal features will have a positive value of 2D curvature and synclinal features will have a negative value of 2D curvature. Second, most of us learned in calculus that the curvature of a function $z(x)$ is simply

$$c_{2D} = \frac{d^2 z}{dx^2} \quad (2)$$

Sigismundi and Soldo show that the peak values of Equation 2 will occur at the crest of a folded 2D image, while the peak values of Equation 1 will occur at the position of tightest curvature having a positive value.

In 3D we encounter somewhat more difficult to visualize formulae. We follow Roberts' notation and assume we fit a

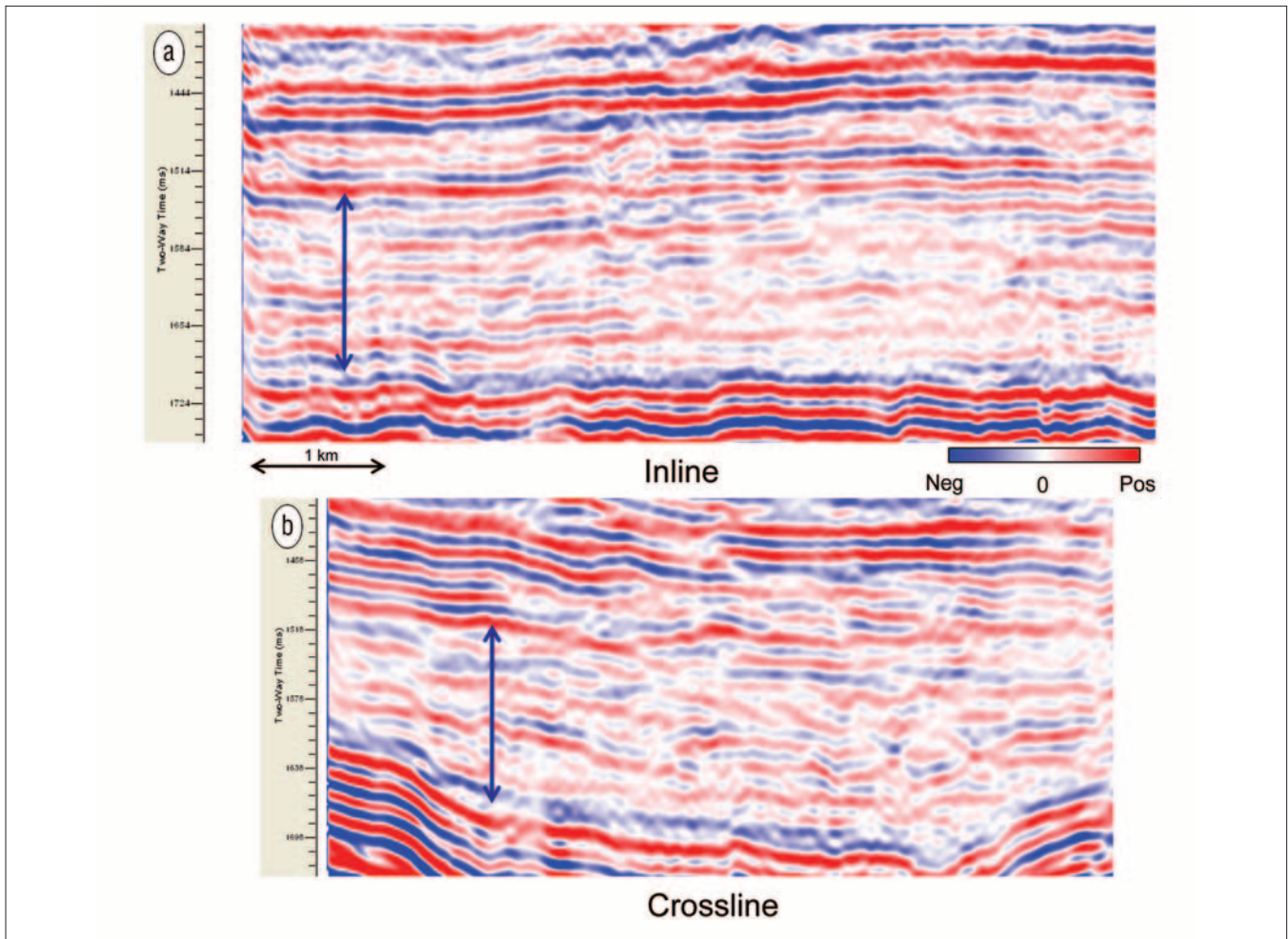


Figure 5. An inline and a crossline from a 3D seismic data volume from Alberta. The vertical blue arrow indicates the fractured zone.

picked horizon with a quadratic surface of the form:

$$z(x,y)=ax^2+cx^2y+by^2+dx+ey+f. \quad (3)$$

Roberts then goes on to define the mean curvature, k_{mean} , Gaussian curvature, k_{Gauss} , and principal curvatures, k_1 and k_2 :

$$k_{mean} = [a(1+e^2)+b(1+d^2)-cde]/(1+d^2+e^2)^{3/2}, \quad (4)$$

$$k_{Gauss} = (4ab-c^2)/(1+d^2+e^2)^2, \quad (5)$$

$$k_1 = k_{mean} + (k_{mean}^2 - k_{Gauss})^{1/2}, \quad (6)$$

$$k_2 = k_{mean} - (k_{mean}^2 - k_{Gauss})^{1/2}, \quad (7)$$

Note that the most-positive principal curvature, k_1 , is a *signed value* that is always greater than or equal to the most-negative principal curvature, k_2 . However, most references on solid geometry (e.g., <http://demonstrations.wolfram.com/EigenvaluesCurvatureAndQuadraticForms/>) define the maximum curvature as the first eigenvalue of a Hessian matrix equation defining the quadratic surface (e.g. Rich, 2008). With this definition, the maximum and minimum curvatures, k_{max} and k_{min} , are

$$k_{max} = \begin{cases} k_1, & \text{if } |k_1| \geq |k_2| \\ k_2, & \text{if } |k_1| < |k_2| \end{cases} \quad (8)$$

$$k_{min} = \begin{cases} k_2, & \text{if } |k_1| \geq |k_2| \\ k_1, & \text{if } |k_1| < |k_2| \end{cases} \quad (9)$$

While these formulae are a 3D generalization of Equation 1, they cause considerable confusion for those who come from a geological (and not mathematical) background. First, the maximum curvature will not always be greater in signed value than the minimum curvature. If we have an elongated synclinal bowl, the maximum curvature will represent the curvature of the tightest cross section, while the minimum curvature will represent the curvature in the strike direction of our basin. For this reason, several authors (including many of our publications) have favored using the most-positive, k_{pos} , and most-negative curvature k_{neg} :

$$k_{pos} = (a+b)+[(a-b)^2+c^2]^{1/2}, \quad (10)$$

$$k_{neg} = (a+b)-[(a-b)^2+c^2]^{1/2}. \quad (11)$$

Equations 6–9 correspond to Equation 1 and Equations 10 and 11 correspond to Equation 2. However, Rich correctly points out that these results are inferior for complex folding. For relatively flat dips, such as encountered in the Fort Worth and Permian Basins of Texas (Al-Dossary and Marfurt, 2006; Blumentritt et al., 2006) $k_{pos} \approx k_1$ and $k_{neg} \approx k_2$.

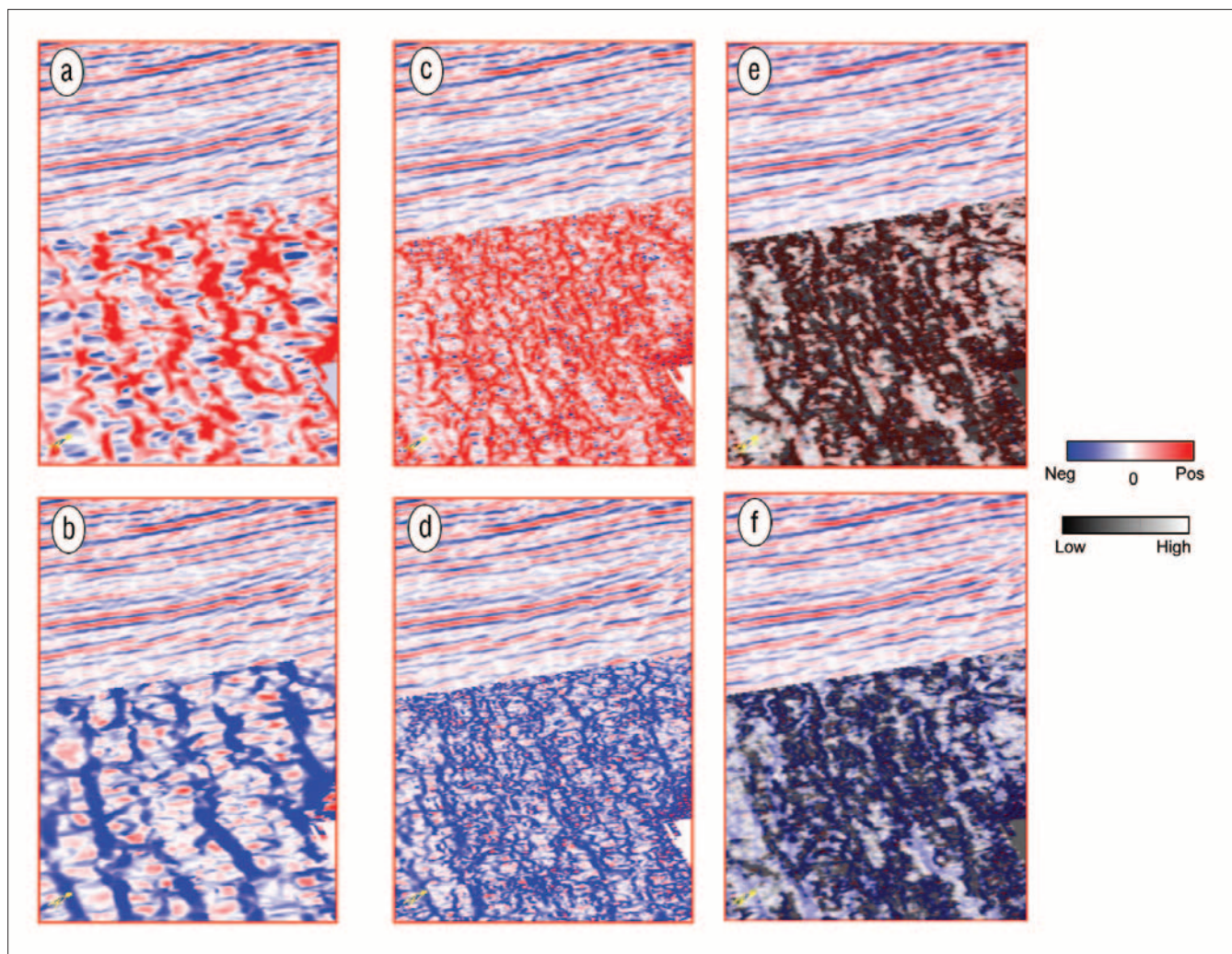


Figure 6. Zoom of chair displays where the vertical display is a portion of a crossline through the original 3D seismic amplitude volume while the horizontal displays are strat slices through (a) most-positive (long-wavelength), (b) most-negative (long-wavelength), (c) most-positive (short-wavelength), and (d) most-negative (short-wavelength) curvature attribute volumes. The lineament detail on the short-wavelength attribute displays is higher and crisper than similar lineaments on the long-wavelength displays. The fault lineaments correlate with the upthrown and downthrown signatures on the seismic amplitude data. Corendering coherence (75% opacity) with (e) short-wavelength most-positive curvature and (f) short-wavelength most-negative curvature shows that the areas of high coherence correlate to planar features which also appear as white on the two curvature images.

However, in highly deformed areas such as the deeper Chicotepec Basin of Mexico (Mai et al., 2009) the differences can be significant. By using the principal curvatures k_1 and k_2 , we maintain the accuracy for highly deformed terranes of k_{max} and k_{min} , while providing the interpretational simplicity of k_{pos} and k_{neg} .

Multispectral volumetric estimation of curvature

Multispectral curvature estimates introduced by Bergbauer et al. (2003) and extended to volumetric calculations by Al Dossary and Marfurt can yield both long- and short-wavelength curvature images, allowing an interpreter to enhance geologic features having different scales. Tight (short-wavelength) curvature often delineates details within intense, highly localized fracture systems. Broad (long-wavelength) curvature often enhances subtle flexures on the scale of 100–200 traces that are difficult to see in conventional seismic,

but are often correlated to fracture zones that are below seismic resolution.

Al Dossary and Marfurt introduced a “fractional derivative” approach for volume computation of multispectral estimates of curvature. They define the fractional derivative as

$$F_{\alpha} \left(\frac{\partial u}{\partial x} \right) = -i(k_x)^{\alpha} F(u), \quad (12)$$

where the operator F denotes the Fourier transform, where u is an inline or crossline component of reflector dip, and where α is a fractional real number that typically ranges between 1 (giving the first derivative) and 0 (giving the Hilbert transform) of the dip. The nomenclature “fractional derivative” was borrowed from Cooper and Cowans (2003); however, an astute mathematician will note that i is not in the parentheses. In this manner we can interpret Equation 12 as simply a low pass filter of the form $k_x^{(\alpha-1)}$ applied to a conven-

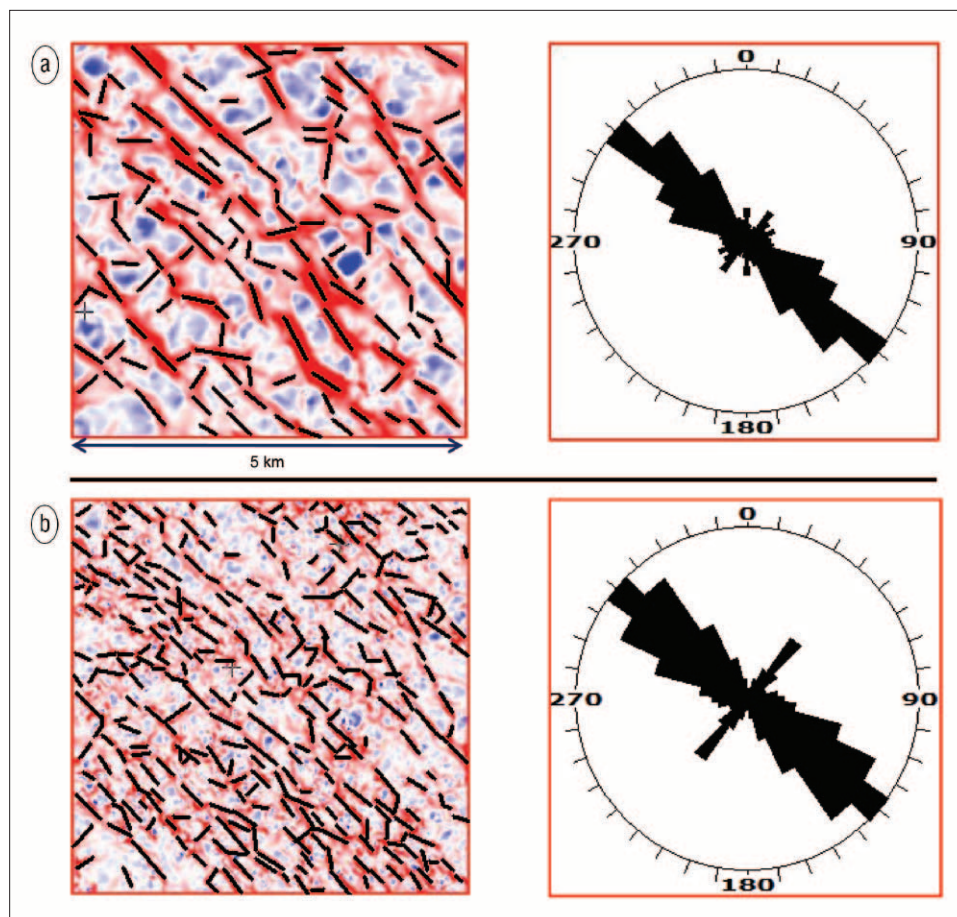


Figure 7. Time slices through the (a) long-wavelength (b) short-wavelength most-positive and most-negative principal curvature volumes. Lineaments interpreted in black are rendered as rose diagrams to the right of each image.

tional first derivative.

The space domain operators corresponding to different values of α mentioned above are convolved with the previously computed dip components estimated at every sample and trace within the seismic volume. In addition, the directional derivative is computed using a 3D spherical rather than a 1D linear operator, thereby avoiding a computational bias associated with the acquisition axes. Lower values of α decrease the contribution of the high wavenumbers, thereby shifting the bandwidth toward longer wavelengths. Figure 2 shows filters for values $\alpha = 0.80$ and 0.25 . Examining these spectral filters, we denote images computed with a value of 0.80 to be “short-wavelength” and 0.25 to be “long-wavelength” curvature results in the figures that follow.

Examples

Appearance of folds and faults. Figure 3 compares a vertical slice through an amplitude volume acquired in Alberta, displayed with horizon slices through volumetric computations of k_{max} , k_{min} , coherence, and k_{max} corendered with coherence. Many interpreters find that k_{max} provides a simple single-attribute image that illuminates the structural curvature often associated with faulting. For horizon-based curvature, such curvature anomalies can be an artifact of fitting a discontin-

uous horizon (overshooting and undershooting) with a smooth quadratic surface. However, with the volumetric curvature images shown in Figure 3, we see that fault-associated curvature anomalies exist in the seismic data. These anomalies may be due to antithetic faulting (e.g., Ferrill and Morris, 2008), to fault drag, to diagenetic alteration of the gauge zone, or other geologic causes. These anomalies may also reflect limitations in seismic data quality such as insufficient vertical resolution or improper imaging due to errors in velocities and statics. Note in Figure 3d that two offset negative curvature grabens are bracketed by low-coherence anomalies on either side. Likewise, low-coherence anomalies bracket a horst feature that appears as a positive curvature anomaly. To the right of the figure, a strong positive curvature anomaly is laterally aligned with a low-coherence anomaly, which we interpret to be a simple flexure. In some places, such as the east side of the southern portion of the graben indicated by the

green arrow, the fault drag is so continuous that coherence no longer detects the fault; however, the fault trend is easily mapped using curvature.

Figure 4 shows corresponding horizon slices through the most-positive curvature, k_{pos} , the most-negative curvature, k_{neg} , and the two principal curvatures k_1 and k_2 , defined by Equations 6 and 7. Note that the most-positive and most-negative curvatures are much more continuous than the maximum and minimum curvatures in Figure 3. For this reason, many authors favor these displays when mapping stratigraphic features (Chopra and Marfurt, 2008) as well as subtle faults and fractures in the presence of gentle dip (e.g., Sullivan et al., 2006; Nissen et al., 2009). However, in areas of folding with significant dip, the crest and trough of a fold defined as the highest and lowest points on a vertical section no longer correspond to the locations of the tightest folding. For this reason, we recommend using the principal curvatures, k_1 and k_2 . We note in Figures 4c and d that the positive and negative curvature anomalies are slightly shifted from those seen in Figures 4a and b. We also note that the information content of Figures 3a and 3b is simply redistributed in Figures 4c and d. In summary, k_1 and k_2 provide the simplicity of interpretation seen in k_{pos} and k_{neg} but retain the robustness of k_{max} and k_{min} in the presence of steep dip.

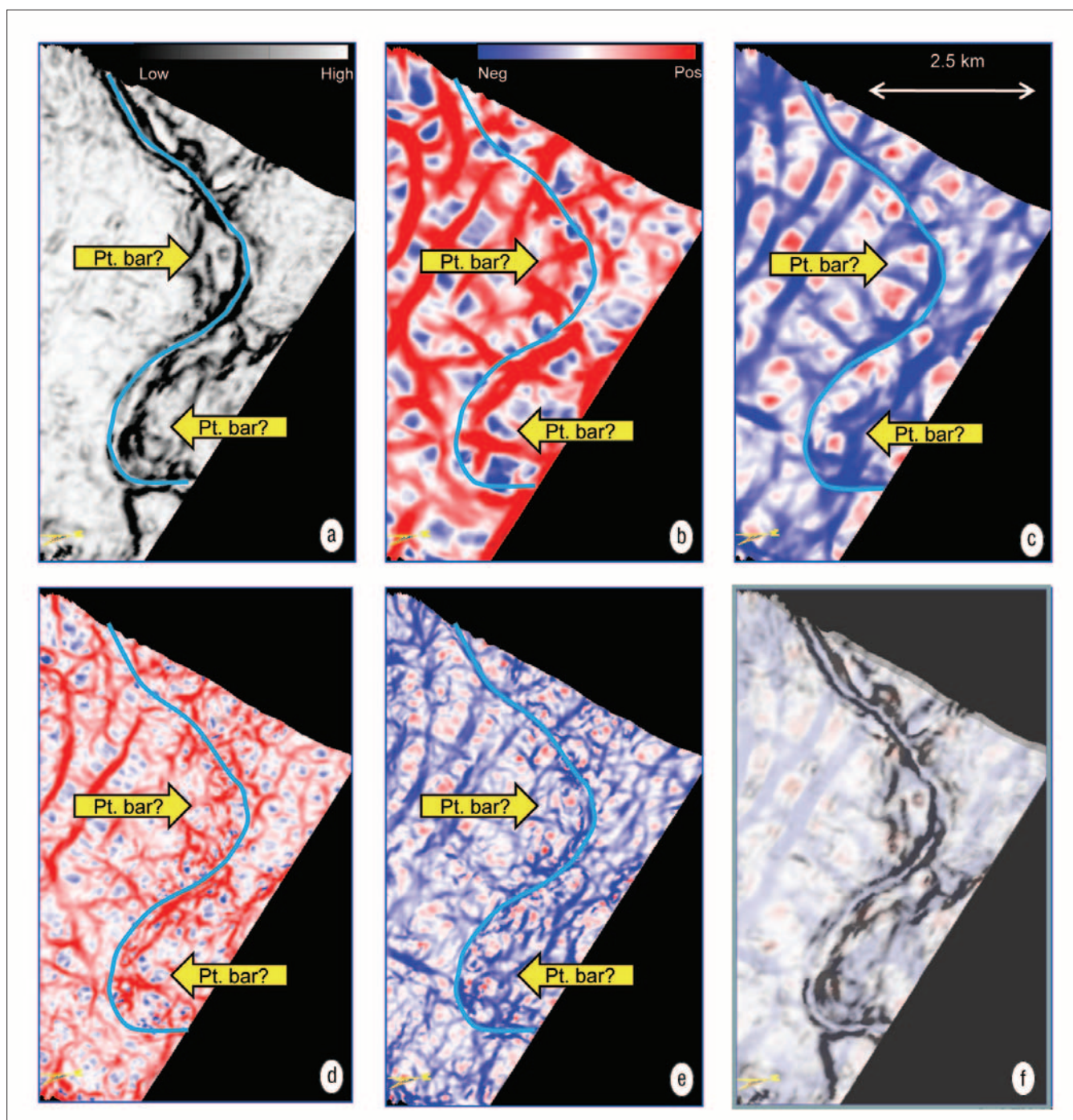


Figure 8. Stratal slices showing an incised channel system through (a) coherence and long-wavelength (b) k_1 and (c) k_2 curvature volumes, followed by short-wavelength (d) k_1 and (e) k_2 volumes. (f) Note the correlation of the channel thalweg seen on long-wavelength k_2 image and the channel edges seen on coherence obtained by corendering the two images (50% opacity on the coherence). Point bars appear as slightly positive curvature anomalies.

Appearance of fractures. In Figure 5, we show an inline and a crossline from a 3D seismic volume from Alberta. This data volume was used for the study of fractures at the level indicated by the blue vertical arrows. The long-wavelength most-positive principal curvature (Figure 6a) indicates the main reflection trends in the form of red lineaments. Areas having negative values of most-positive principal curvature displayed as blue correspond to structural bowls. The long wavelength most-negative principal curvature (Figure 6b) exhibits a sim-

ilar, but laterally shifted pattern of blue lineaments. Areas having positive values of most-negative principal curvature displayed as red correspond to structural domes. The overall structural pattern therefore has an “egg-carton” appearance, which we interpret to be due to two nearly perpendicular sets of faults and/or folds. The short-wavelength versions of these displays are shown in Figures 6c and 6d, which provide greater detail of our dense fault and fracture network. Figures 6e and f show the short-wavelength curvature images

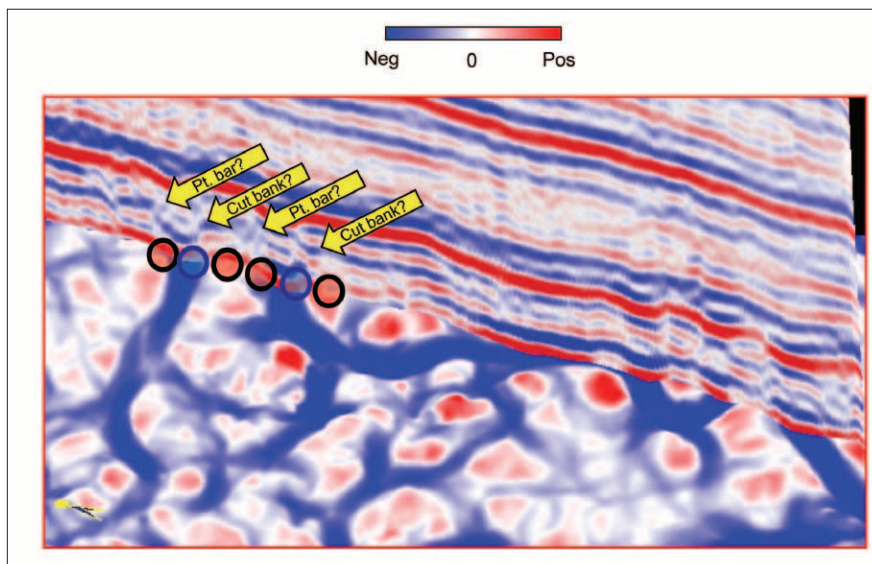


Figure 9. Zoomed image of a vertical slice through seismic amplitude and long-wavelength k_2 curvature. Red and blue circles indicate positive and negative values of curvature seen on the vertical seismic section. In this case, negative curvature delineates the thalweg, or channel axis, while positive curvature delineates the point bar corresponding to the handle of the frying-pan-shaped channel anomaly seen on the vertical seismic.

overlain by the corresponding coherence images rendered with the opacity set to 75%. Note that the high-coherence portions of the image appear as white rather than as red or blue, indicating the more planar features are continuous, while the areas of higher deformation (folding or faulting) are discontinuous.

Ideally, we want to calibrate fracture predictions from curvature images to fracture or stress measures made using log data. One promising way is to interpret the lineaments in a fractured zone and then transform them into a rose diagram. Such rose diagrams can then be compared with similar rose diagrams from image well logs to gain confidence in the seismic-to-well calibration. Once a favorable match is obtained, the interpretation of fault/fracture orientations and the thicknesses over which they extend can be used with greater confidence

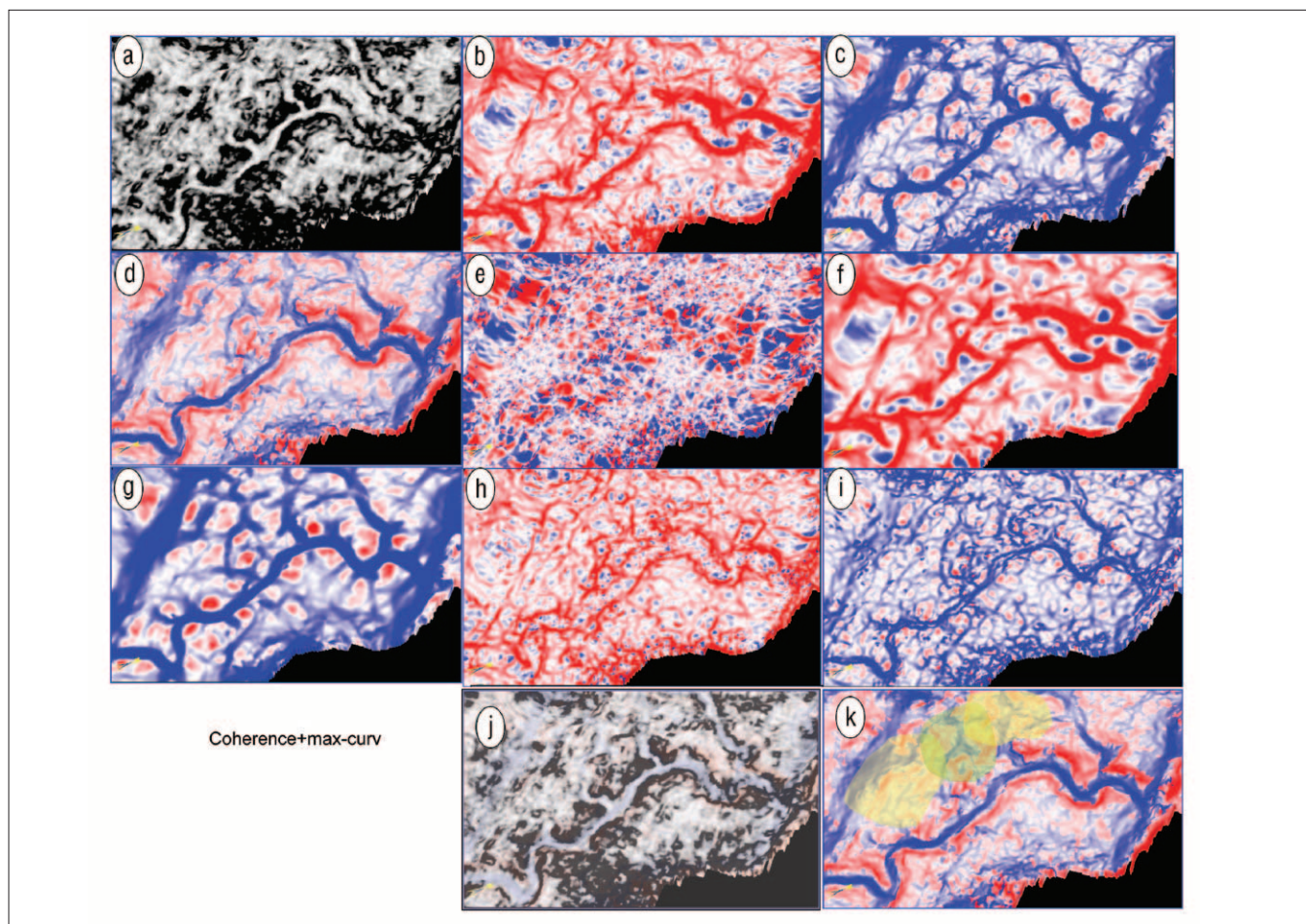


Figure 10. Stratal slices showing an incised channel system through (a) coherence, (b) k_1 (long-wavelength), (c) k_2 (long-wavelength), (d) k_{\max} , (e) k_{\min} , (f) most-positive curvature (long-wavelength), (g) most-negative curvature (long-wavelength), (h) most-positive curvature (short-wavelength), (i) most-negative curvature (short-wavelength), and (j) corendered coherence (50% opacity) and k_2 (long-wavelength) volumes through an incised channels system seen on a different survey acquired in Alberta, Canada. Applying concepts of seismic stratigraphy, we interpret a main channel and at least three crevasse-splay features resulting in planar to slightly positive fan features (k).

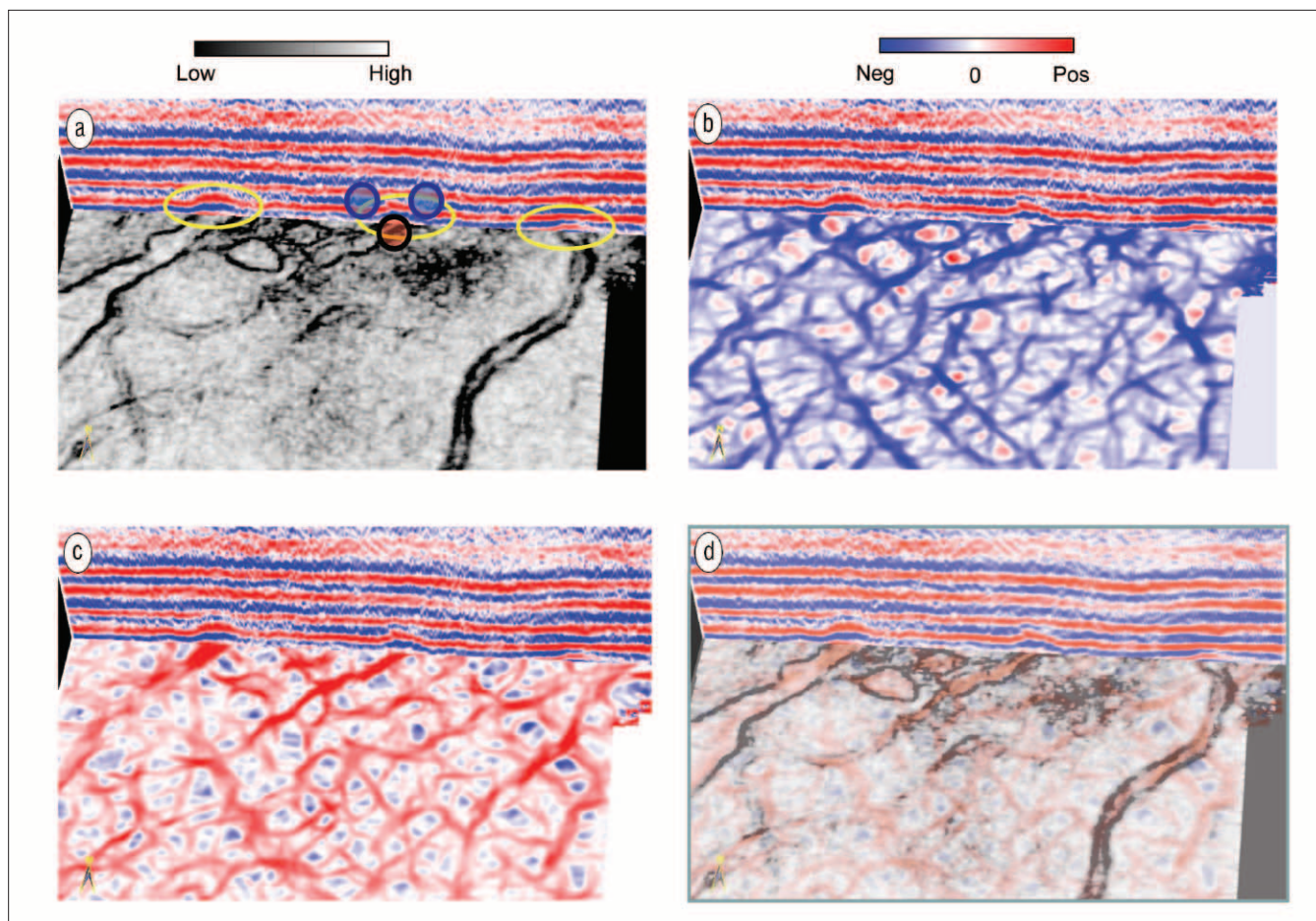


Figure 11. Not all incised valleys result in negative curvature anomalies. In this example from Alberta, we see positive features associated with the channel axes indicating that the channel is filled with sand and the surrounding matrix consisting of a more easily compactable shale. (a) Coherence, (b) long-wavelength k_1 , (c) long-wavelength k_2 , and (d) corendered coherence (50% opacity) and long-wavelength k_1 volumes.

for more quantitative reservoir analysis. Needless to say such calibrations should be carried out in localized areas around the wells for accurate comparisons.

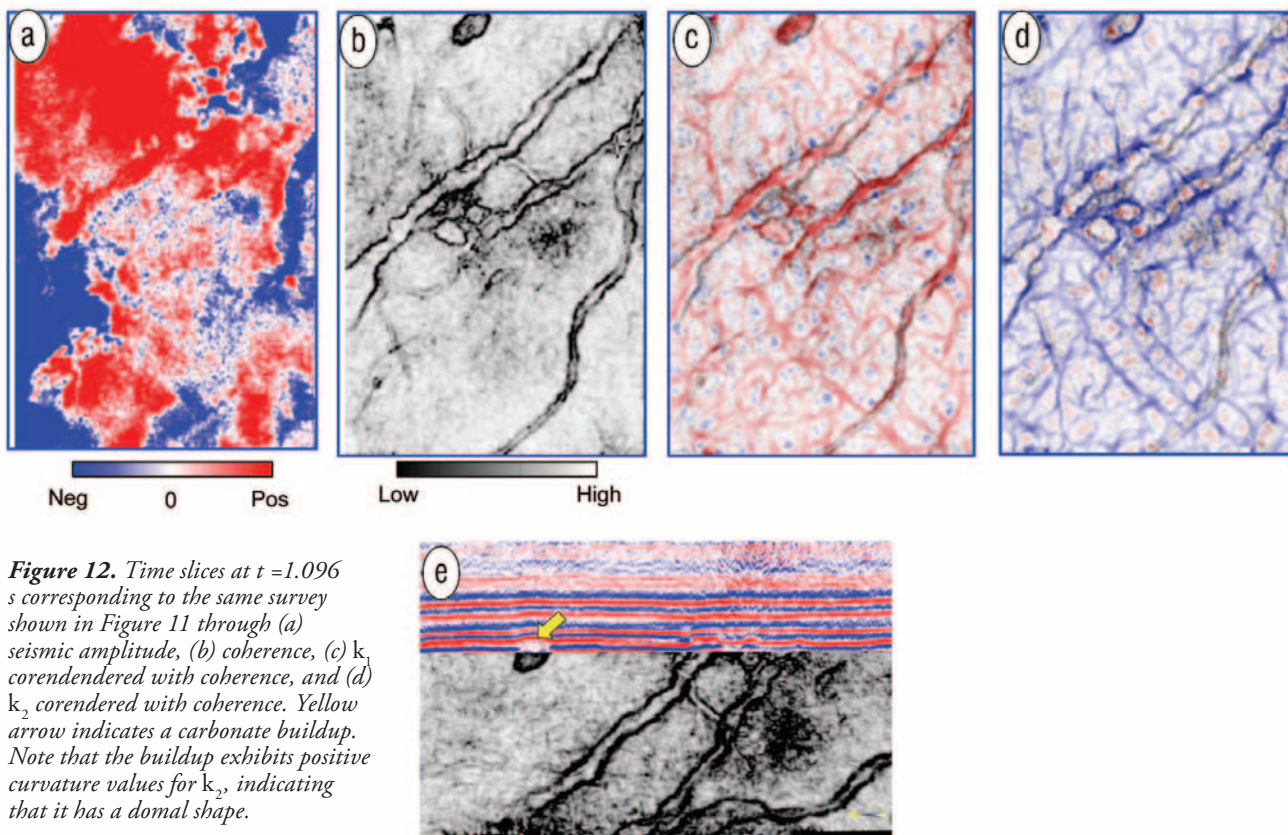
Figure 7 shows a simple workflow to quantify the structural fabric seen on coherence and curvature images. Windowing in on a zone of interest, the interpreter simply picks ridges on the long-wavelength or short-wavelength most-positive principal curvature images (or valleys on the most-negative principal curvature images) and generates a rose diagram. Notice in this example the rose diagram generated from the short-wavelength curvature display leads to a more cleanly defined display showing two major axes of structural deformation.

Appearance of incised channels. Figure 8 compares coherence with the long-wavelength and short-wavelength versions of the most-positive and negative principal curvatures. Notice a meandering channel on the coherence display (Figure 8a). Figures 8b and 8c show the long-wavelength most positive and most negative principal curvatures. The axis or the thalweg of the channel is seen clearly on the long-wavelength version of the most-negative curvature. The point bars appear as local structural highs on the most-positive curvature. As expected, enhanced resolution in terms of definition of the channel is seen on the short-wavelength version of both the

most-positive and most-negative principal curvatures (Figures 8d and 8e). There is an excellent correlation between the valley-shaped anomaly seen on the long-wavelength most negative principal curvature and coherence (Figure 8f).

We correlate the edges of the incised channel system seen on attributes using the chair display in Figure 9. Note the two classic frying-pan-shaped anomalies seen just above the picked horizon on the vertical slice through the seismic amplitude. Note also the negative curvature anomalies in k_2 correspond to the thalweg (blue circles on the vertical seismic) while the positive anomalies in k_1 correspond to the point-bar side of the channel (red circles on the vertical seismic).

Another comparison of coherence with the long-wavelength and short-wavelength versions of the most-positive and negative principal curvature for the channel is shown in Figure 10. Note, in the coherence image in Figure 10a, that this channel appears to have several more crevasse-splays than the channel showed in the previous image. Again, notice that the thalweg of the channel is well-defined on the most-negative principal curvature and the edges or the levees of the channel can be clearly marked on the most-positive curvature. In Figure 10j, we plot the coherence on the maximum curvature using an opacity value of 50%. We note that the channel axis and crevasse splays appear as high-coherent,



valley-shaped events. We interpret the relatively high coherent, flat to slightly positive curvature events at the ends of the crevasse splays to be corresponding fans (Figure 10k).

Differential compaction. The two previous channel images showed negative curvature anomalies associated with the channel axis, a feature that is consistent with differential compaction over a shale-filled incised valley. Not all channels result in negative curvature anomalies. The feature in Figure 11 clearly appears to be a channel on the coherence image, but appears as a positive curvature anomaly along the channel axis. We interpret this anomaly to be due to differential compaction over a sand-filled channel incised in a shale matrix, resulting in a local high. Such anomalies are common in the North Sea and other parts of the world where sufficient time has passed to produce differential compaction.

We also see differential compaction of sediments about more rigid carbonate buildups (Figure 12). In this image, we can recognize the mound by its circular outline on coherence, low-amplitude internal reflectivity, domal shape indicated by the two curvature volumes, k_1 and k_2 , and deformation of overlying sediments due to differential compaction.

Conclusions

Volumetric curvature is a well-established interpretational tool that allows us to image subtle faults, folds, incised channels, differential compaction, and a wide range of other stratigraphic features. The maximum and minimum curvatures define the eigenvalues of a quadratic surface. By defini-

tion (and based on eigenstructure analysis), the maximum curvature is defined as the principal curvature that has the larger absolute value. We find that the principal curvatures k_1 and k_2 , where $k_1 \geq k_2$, provide the simplicity of interpretation seen in k_{pos} and k_{neg} , but retain the robustness of k_{max} and k_{min} in the presence of steep dip.

Multispectral volumetric curvature attributes are valuable for prediction of fracture lineaments in deformed strata. Several applications of volume curvature have been completed in different geological settings, which are useful for different stratigraphic features, ranging from imaging of channel boundaries and small scale faults to highly fractured zones. Corendering volumetric curvature with coherence provides a particularly powerful tool. **TLE**

References

- Al-Dossary, S. and K. J. Marfurt, 2006, 3D volumetric multispectral estimates of reflector curvature and rotation: *Geophysics*, **71**, P41–51.
- Barnes, A. E., 2000, Weighted average seismic attributes: *Geophysics*, **65**, 275–285.
- Bergbauer, S., T. Mukerji, and P. Hennings, 2003, Improving curvature analyses of deformed horizons using scale-dependent filtering techniques: *AAPG Bulletin*, **87**, 1255–1272.
- Blumentritt, C., K. J. Marfurt, and E. C. Sullivan, 2006, Volume-based curvature computations illuminate fracture orientations, Lower-Mid Paleozoic, Central Basin Platform, West Texas: *Geophysics*, **71**, B159–B166.
- Chopra, S. and K. J. Marfurt, 2008, Emerging and future trends in

- seismic attributes: The Leading Edge, **27**, 298–318.
- Cooper, G. R. J. and D. R. Cowans, 2003, Sunshading geophysical data using fractional order horizontal gradients, The Leading Edge, **22**, 204–205.
- Ferrill, D. A. and A. P. Morris, 2008, Fault zone deformation controlled by carbonate mechanical stratigraphy, Balcones fault system, Texas, AAPG Bulletin, **92**, 359–380.
- Fomel, S., 2008, Predictive painting of 3D seismic volumes: 77th Annual International Meeting, SEG, Expanded Abstracts, 864–868.
- Hart, B. S., R. Pearson, and G. C. Rawling, 2002, 3D seismic horizon-based approaches to fracture-swarm sweet-spot definition in tight-gas reservoirs: The Leading Edge, **21**, 28–35.
- Hart, B. S. and J. Sagan, 2005, Horizon attribute curvature aids stratigraphic interpretation: AAPG Search and Discovery, article 40172, <http://www.searchanddiscovery.com/documents/2005/hart/index.htm>.
- Lisle, R. J., 1994, Detection of zones of abnormal strains in structures using Gaussian curvature analysis: AAPG Bulletin, **78**, 1811–1819.
- Marfurt, K. J., 2006, Robust estimates of reflector dip and azimuth: Geophysics, **71**, 29–40.
- Mai, H., K. J. Marfurt, and S. Chavez-Perez, 2009, Coherence and volumetric curvatures and their spatial relationship to faults and folds, an example from Chicontepec basin, Mexico: 78th Annual International Meeting, SEG, Expanded Abstracts, 1063.
- Nissen, S. E., T. R. Carr, K. J. Marfurt, and E. C. Sullivan, 2009, Using 3D seismic volumetric curvature attributes to identify fracture trends in a depleted Mississippian carbonate reservoir: Implications for assessing candidates for CO₂ sequestration, in M. Grobe, J. C. Pashin, and R. L. Dodge, eds., Carbon dioxide sequestration in geological media—State of the science: AAPG Studies in Geology, **59**, 297–319.
- Randen, T. E. Monsen, C. Signer, A. Abrahamsen, J. O. Hansen, T. Saeter, J. Schlaf, and L. Sønneland, 2000, Three-dimensional texture attributes for seismic data analysis: 70th Annual International Meeting, SEG, Expanded Abstracts, 668–671.
- Rich, J., 2008, Expanding the applicability of curvature attributes through clarification of ambiguities in derivation and terminology: 77th Annual International Meeting, SEG, Expanded Abstracts, 884–887.
- Roberts, A., 2001, Curvature attributes and their application to 3D interpreted horizons: First Break, **19**, 85–99.
- Sigismondi, E. M., and C. J. Soldo, 2003, Curvature attributes and seismic interpretation: Case studies from Argentina basins: The Leading Edge, **22**, 1122–1126.
- Sullivan, E. C., K. J. Marfurt, A. Lacazette, and M. Ammerman, 2006, Application of new seismic attributes to collapse chimneys in the Fort Worth Basin: Geophysics, **71**, B111–B119.

Acknowledgment: We thank Arcis Corporation for permission to publish this work.

Corresponding author: schopra@arcis.com